Physics of the Earth and Planetary Interiors 305 (2020) 106490

Contents lists available at ScienceDirect

Physics of the Earth and Planetary Interiors

journal homepage: www.elsevier.com/locate/pepi

Mineralogy and density of Archean volcanic crust in the mantle transition zone

Byeongkwan Ko[a,*], Vitali Prakapenka[b], Martin Kunz[c], Clemens Prescher[b,d], Kurt Leinenweber[a], Sang-Heon Shim[a,*]

[a] School of Earth and Space Exploration, Arizona State University, Tempe, AZ 85287, United States
[b] Center for Advanced Radiation Sources, University of Chicago, Chicago, IL 60439, United States
[c] Advanced Light Source, Lawrence Berkeley National Laboratory, Berkeley, California 94720, United States
[d] Now at Photon Sciences, Deutsches Elektronen-Synchrotron (DESY), Hamburg 22607, Germany

ARTICLE INFO

Keywords:
Archean volcanic crust
Density
Mineralogy
Mantle transition zone
In-situ X-ray diffraction
High *P*–*T* experiments

ABSTRACT

The composition of Archean volcanic crust can be characterized by a higher Mg/Si ratio than modern mid-ocean ridge basalt (MORB), because of the higher degree melting from the warmer mantle in the Archean. Although modern MORB may become less dense than the surrounding mantle beneath the mantle transition zone (MTZ), the Mg-rich composition of Archean volcanic crust may result in the different density, and therefore different sinking behavior near the MTZ. In order to understand the compositional effect of Archean volcanic crust on the sinking behaviors and the scale of mantle mixing in the Archean, we investigated the mineralogy and density of Archean volcanic crust near the MTZ (470–910 km-depth). We conducted experiments at 19–34 GPa and 1400–2400 K using the laser-heated diamond anvil cell (LHDAC) combined with in-situ X-ray diffraction (XRD). The in-situ XRD and the chemical analysis revealed that Archean volcanic crust forms garnet and ringwoodite (84 and 16 vol%, respectively), which gradually transforms to Brg and CaPv (82 and 18 vol%, respectively) at 23–25 GPa and 1800 K. Our in-situ XRD experiments allowed us to measure the volumes of stable phases and to estimate their densities at high pressure and temperature. The results suggest that Archean volcanic crust maintains greater density than the pyrolitic mantle in the Archean regardless of temperature at 20–34 GPa (570–850 km-depth), promoting further sinking into the deeper mantle in the Archean. We also considered the density of the subducting slab in the Archean. The density model showed that the subducting slab is still denser or at least equally dense as the surrounding pyrolitic mantle in the Archean.

1. Introduction

Surface materials have been transported into the deep mantle and played vital roles in mantle geochemistry and dynamics for billions of years in the Earth's history (e.g., Van Hunen and Moyen, 2012; Laurent et al., 2014; Tang et al., 2016; Condie, 2018). Seismic tomography images have shown stagnation of the slabs beneath the mantle transition zone (MTZ) in the Western Pacific (e.g., van der Hilst and Seno, 1993; Fukao et al., 2009; Li and McNamara, 2013; King et al., 2015). Indeed, sinking of the slabs into the deep mantle can be challenged beneath the MTZ at 670–760 km-depth (Christensen, 1997; Ogawa, 2003; Davies, 2008; Klein et al., 2017) where the density of the surrounding mantle increases dramatically because of the post-spinel transition (Hirose, 2002; Ye et al., 2014; Ishii et al., 2018).

While the density of the modern subductig slab has been well documented at high pressures and high temperatures (Hirose et al., 1999; Irifune and Ringwood, 1993; Ringwood and Irifune, 1988), the density of the early Earth's materials is not the case. In the Archean, the mantle potential temperature was likely much greater than present day by approximately 200 K (Korenaga, 2008; Herzberg et al., 2010). The high temperature results in the more extensive partial melting in the Archean, resulting in two important differences for Archean volcanic crust. First, Archean volcanic crust forms with a much greater MgO content than present-day mid ocean ridge basalt (MORB; Table 1) (Herzberg et al., 2007, 2010). The different composition of Archean volcanic crust would lead to different mineralogy and density at high pressure-temperature (*P*–*T*) conditions in the mantle. Second, the thickness of the crust should be much greater in the Archean (up to 45 km-thick) than in the modern day (7 km-thick; Herzberg et al., 2010; Herzberg and Rudnick, 2012). With the large thickness, Archean

---

* Corresponding authors.
E-mail addresses: byeongkw@asu.edu (B. Ko), SHDShim@asu.edu (S.-H. Shim).

https://doi.org/10.1016/j.pepi.2020.106490
Received 24 October 2019; Received in revised form 19 March 2020; Accepted 8 April 2020

Table 1
Chemical compositions of pyrolite, basaltic crust, complementary residues, and Archean volcanic crust. After excluding minor elements, we normalized each composition to 100%.

wt%	Pyrolite[a]	B30[b]	Modern MORB[c]	Archean residue[b]	Modern residue[d]	Archean crust[e]
SiO_2	45.1	47.0	51.8	43.8	43.4	47.6
Al_2O_3	4.8	7.5	15.5	2.8	1.3	7.1
FeO[†]	8.4	12.7	10.1	6.4	8.6	12.3
MgO	37.7	22.8	8.0	46.3	45.7	22.9
CaO	3.5	8.8	11.7	0.8	0.9	8.3
Na_2O	0.4	1.3	2.1	0	0	1.7
Mg#[‡]	88.9	76.2	58.5	92.8	90.4	76.8
(Mg + Fe + Ca)/Si	1.49	1.15	0.63	1.72	1.76	1.12
Thickness (km)[§]	–	40	7	74	32	–

[a] Composition obtained from McDonough and Sun (1995).
[b] Modeled compositions obtained from Johnson et al. (2014). B30 was used for experiments in this study.
[c] Composition obtained from Gale et al. (2013).
[d] Composition obtained from Baker and Beckett (1999).
[e] Oceanic plateau basalt 3.3 Ga; Schulz (1982).
† All Fe in B30 is assumed to exist as FeO.
‡ Mg# = Mg/(Mg + Fe).
§ Thickness of a layer in the subducting slab considered in this study.

volcanic crust takes a large portion of the subducting slab in the Archean, and therefore plays a more important role in the sinking behavior of the subducting slab.

Archean volcanic crust could have been transported into the mantle through a range of different processes: delamination (e.g., Bédard, 2006; Johnson et al., 2014), and subduction (e.g., Laurent et al., 2014; Tang et al., 2016; Condie, 2018). For the case of subduction, timing for the onset of modern-style plate tectonics is still under debate. Multiple lines of geochemical evidence suggest that modern-style global subduction would have occurred since 2.0–3.5 Ga (Laurent et al., 2014; Tang et al., 2016; Condie, 2018). Subduction style in the Archean could have been episodic (Van Hunen and Moyen, 2012). Geodynamic modeling has shown that the hotter mantle in the Archean results in weak subducting slabs, leading to frequent break-off of the slabs (Van Hunen and Moyen, 2012).

If Archean volcanic crust remains as a heterogeneity in the present-day mantle owing to the slow chemical diffusion at high pressure (Holzapfel et al., 2005; Stixrude and Lithgow-Bertelloni, 2012; Xu et al., 2011; Ito and Toriumi, 2010), the behavior of such heterogeneity is also important for understanding the origin of the seismic heterogeneities found in the mantle (e.g. Fukao et al., 2009; Fukao and Obayashi, 2013; Wu et al., 2019).

It is also of interest if Archean volcanic crust would have contributed to the rise of atmospheric O_2 at approximately 2.4 Ga (the Great Oxidation Event or GOE) (Kasting, 2013). The MgO-rich composition might have resulted in the more extensive H_2 production through serpentinization than in the modern day (Kasting, 2013). The compositional change in the volcanic crust during the mantle cooling might have reduced such H_2 production, leading to the accumulation of O_2 in the atmosphere. In addition, the recent measurements of the V partitioning in ancient volcanic rocks suggested that the reducing Archean upper mantle might have undergone the secular oxidation between 3.5 and 1.9 Ga (Nicklas et al., 2019). Possible mechanisms for the oxidation processes include not only the compositional change of the volcanic crust recycled into the mantle, but also homogenization of the redox state of the mantle by effective mantle mixing (Nicklas et al., 2019; Aulbach and Stagno, 2016). The style of the mantle convection in the Archean could have been also affected by the changes in the tectonic mode. It is possible that the subducting slabs might have facilitated the whole mantle mixing with the primordial oxidizing materials stored in the lower mantle (Nicklas et al., 2019; Aulbach and Stagno, 2016; Andrault et al., 2018a).

The composition of the Archean materials sunken to the mantle has been modeled with komatiitic compositions (e.g. Nishihara and Takahashi, 2001; Klein et al., 2017). Nishihara and Takahashi (2001) conducted multi-anvil experiments and calculated the density of komatiite with thermodynamic parameters and the calculated zero-pressure densities of the synthesized phases. They showed that the density of komatiite is greater than the PREM density in the MTZ up to 23 GPa. The density of the surrounding mantle in the Archean is likely lower than the PREM density (i.e., present-day mantle density) because of the higher temperature. Therefore, the density contrast between their komatiite and the Archean mantle may be even greater. However, their komatiite composition may not be representative Archean volcanic crust formed by partial melting of the mantle, because of the higher MgO content (32 wt%) and the lower Al_2O_3 content (4 wt%) compared to non-arc basaltic compositions in the Archean (23 and 9 wt%, respectively; Herzberg et al., 2010; Johnson et al., 2014; Table 1). Furthermore, the density was not directly measured at high *P*–*T*.

Klein et al. (2017) has recently studied the density of komatiitic composition at depths of the MTZ and the topmost lower mantle using a thermodynamic modeling program, Perple_X (Connolly, 2009). They used a less MgO-rich komatiitic composition (26 wt% of MgO) for Archean volcanic crust (Herzberg et al., 2010). The model predicted that komatiite is denser than the pyrolitic Archean mantle in the MTZ and the topmost lower mantle, supporting the likelihood of the sinking of the materials into the lower mantle.

However, unlike other compositions, such as modern MORB and pyrolite which have been cross-examined by theoretical calculations (Xu et al., 2008; Stixrude and Lithgow-Bertelloni, 2012) and in-situ experiments (Ricolleau et al., 2010; Hirose et al., 2005), the density of the Archean volcanic crustal composition has not been directly measured by in-situ experiments. Also, it would be worthwhile to explore differences in mineralogy and density between komatiite and modeled compositions (Johnson et al., 2014) for Archean volcanic crust. More importantly, no study has explored the combined density of the crust and harzburgitic layer for the Archean subducting slabs. The lack of such consideration limits our understanding of the sinking behaviors of the Archean subducting slabs.

As mentioned above, Archean volcanic crust is different from modern MORB in two aspects: 1) much more MgO-rich composition and 2) greater thickness (Korenaga, 2008; Herzberg et al., 2010). Because of these differences, Archean volcanic crust would have played a different role in the sinking behaviors of the Archean subducting slabs than modern MORB does. It would be particularly important to address a question of how sinking behaviors of subducting slabs may have evolved over time as Earth's mantle cools.

Here, we report experimental results on the composition for Archean volcanic crust at pressures of 19–34 GPa and temperatures of 1400–2400 K. Our in-situ X-ray diffraction provides direct measurements of the unit-cell volumes of the stable phases, allowing us to estimate the densities at high *P*–*T*. We also explored the effects of harzburgite layer using Perple_X, for the case where Archean volcanic crust is transported to the MTZ through subduction style.

2. Experimental methods

2.1. Starting material

We synthesized a homogeneous glass using the laser-levitation method (Tangeman et al., 2001) under a reducing condition (1:1 ratio of the gas mixture $CO:CO_2$). The chemical composition of the starting material was obtained from the partial melting model by Johnson et al. (2014) (Table 1). The model assumes that the MgO and FeO contents of the crustal composition linearly increase with an increase in the mantle potential temperature (T_P) based on the reported chemical compositions of a range of non-arc volcanic crustal compositions from 3.5 Ga to the present day (Johnson et al., 2014; Herzberg et al., 2007, 2010; Palin and White, 2016). From this model, we chose the composition for Archean volcanic crust (2.5–3.0 Ga; hereafter B30) that might have formed at a T_P of ~1900 K. We confirmed successful synthesis of the starting material in an electron probe micro analyzer (JEOL JXA-8530F EPMA) combined with wavelength-dispersive X-ray spectrometer (WDS) at Arizona State University (ASU) (Table 1). We did not measure the $Fe^{3+}/\Sigma Fe$ in the starting material.

2.2. Laser-heated diamond-anvil cell experiments

The powdered glass was mixed with ~10 wt% of Au powder (grain size of 1–3 μm), which served as a pressure standard and a laser absorber in the laser-heated diamond-anvil cell (LHDAC) experiments. The mixture was compressed to thin foils with a size of 100–200 μm and a thickness of ~10 μm. Then, the foil was loaded into a hole in a pre-indented rhenium gasket with a micro-manipulator (Microsupport Axis Pro SS) at ASU. We placed four spacers (< 10 μm sized pure sample particle) between the sample foil and each side of the diamond culets for the gas or liquid medium loading. We loaded Ne and Ar in the COMPRES-GSECARS high-pressure gas loading system (Rivers et al., 2008) or the cryogenic liquid loading system at ASU. For the solid media (NaCl and KCl), powder was dried at 120 °C for 4 h before loading. The solid media were prepared as foils and placed below and above the sample foil in the sample chamber. We compressed the samples in the symmetric-type diamond-anvil cell. The samples were compressed with diamond anvils (400 μm-sized culet).

We have conducted LHDAC experiments combined with in-situ X-ray diffraction (XRD) at sector 13-IDD of the GeoSoilEnviroConsortium (GSECARS) in the Advanced Photon Source (APS) (Prakapenka et al., 2008) (Tables S1 and S2). The pressure and temperature ranges of the experiments were 19–34 GPa and 1400–2400 K, respectively. For run #4430 only, we synthesized the sample in LHDAC at ASU and then measured diffraction patterns at high pressure and room temperature in DAC at sector 12.2.2 in the Advanced Light Source (ALS) (Table S1). The wavelengths of the monochromatic X-ray beams were 0.3344, 0.4133, and 0.4959 Å for GSECARS and 0.4971 Å for ALS. For in-situ experiments, we focused the laser beams on both sides of the sample and aligned the laser beams coaxially with the X-ray beam by visually observing X-ray fluorescence, in order to measure XRD patterns at the center of the laser heating spot. Typical beam diameters for the X-ray focus and the laser hotspot on the sample in LHDAC were ~5 and 20 μm, respectively. We fit the thermal radiation spectra measured from both sides of the sample to Planck gray-body equation for the estimation of temperature. We attached a gas membrane to the LHDAC for fine control of pressure during in-situ laser heating (Letoullec et al., 1988), except for run #218 where the pressure was increased manually to the target pressure.

We measured diffraction images using a MarCCD or a Dectris Pilatus detector at GSECARS. For run #4430, diffraction images were collected with a Mar345 detector at ALS. The diffraction images were integrated to 1D diffraction patterns with the calibration parameters obtained from the LaB_6 standard in the DIOPTAS software (Prescher and Prakapenka, 2015). Diffraction images were collected for 5–10 s to ensure enough quality for data analysis. For run #4430 at ALS, we exposed the detector for 120–300 s. The collected diffraction patterns were analyzed and fitted with a pseudo-Voigt profile function to obtain the peak positions in the PeakPo software (Shim, 2017a). We obtained unit-cell parameters using the PeakPo and UnitCell softwares (Holland and Redfern, 1997). We determined pressures with the equation of state (EOS) of Au (Dorogokupets and Dewaele, 2007) using the Pytheos software (Shim, 2017b). The pressures at high temperatures were further corrected according to Ye et al. (2017). The unit-cell volume of Au was calculated from the 2–5 diffraction lines for majority of the data points.

We heated multiple spots in each sample and avoided areas that are close to the Re gasket. For each heating spot, an area with a diameter of 20 μm was heated for up to 11 min (Table S1). The locations of heating spots were chosen with an enough distance up to 30 μm from the previously heated areas in order to start a new heating cycle with unheated fresh areas.

In-situ XRD patterns showed that our glass sample transformed into crystalline phases within 5–60 s depending on temperature. Once formed, the XRD peak intensities of crystalline phases gradually grow over time without significant changes in the further heating. For most runs, the laser power was first increased at a previously heated spot until a target temperature is reached, and then instantly translated to an unheated amorphous area such that the new area can reach target temperature directly. This heating method helps preventing kinetic effects because the amorphous starting material does not experience low temperatures during gradual increase in laser power in typical laser-heating experiments.

2.3. Chemical analysis

We recovered the synthesized samples from runs #218 and #4430 in a micro-manipulator. The samples were processed for the STEM measurements in a focused ion beam (FIB; FEI Nova 200 and FEI Helios) at ASU and University of Arizona (UofA), respectively. We extracted the center part of the heated area and mounted it on a Cu or Mo grid. The composition of the sample was analyzed in the aberration-corrected scanning transmission electron microscope (STEM): JEOL ARM200F at ASU and Hitachi HF-5000 at UofA combined with energy-dispersive X-ray spectroscopy (EDS). A 120 and 200 keV of acceleration voltages were used at ASU and UofA, respectively. We measured standard spectra from the starting glass material for the data analysis. We performed a 2D chemical mapping for run #4430 and then estimated volume fractions of phases from the area fraction (Fig. 1). We also performed a point analysis with exposure time of 20–40 s depending on the beam sensitivity at a target grain. The collected EDS spectra were fitted using a python code LMFIT (Newville et al., 2016).

3. Experimental results

We have found three distinct *P*–*T* fields with different mineralogy in our experiments (Fig. 2): garnet-dominant (Gt-dominant), garnet-bridgmanite-transition (Gt-Brg-transition), and bridgmanite-dominant (Brg-dominant) *P*–*T* fields (Fig. 3).

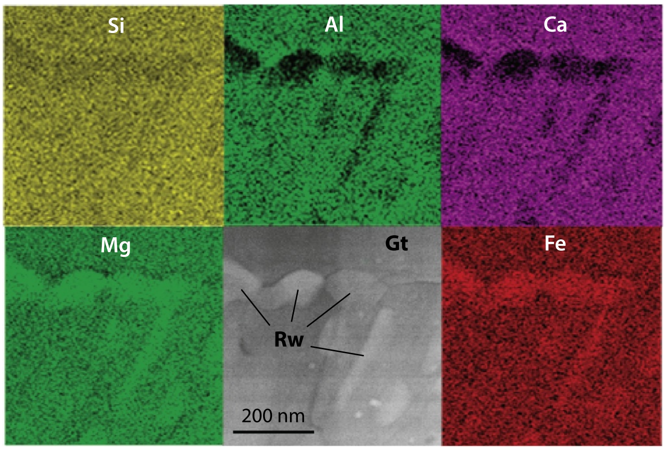

Fig. 1. A high-angle annular dark-field image in the different region with chemical maps of B30 in LHDAC. The sample was synthesized at 19.5 GPa and 1900 K. The brighter colour in each chemical map represents the more concentration of the corresponding element. The chemical compositions and the proportions of individual phases are provided in Table 2. Gt: garnet; Rw: ringwoodite.

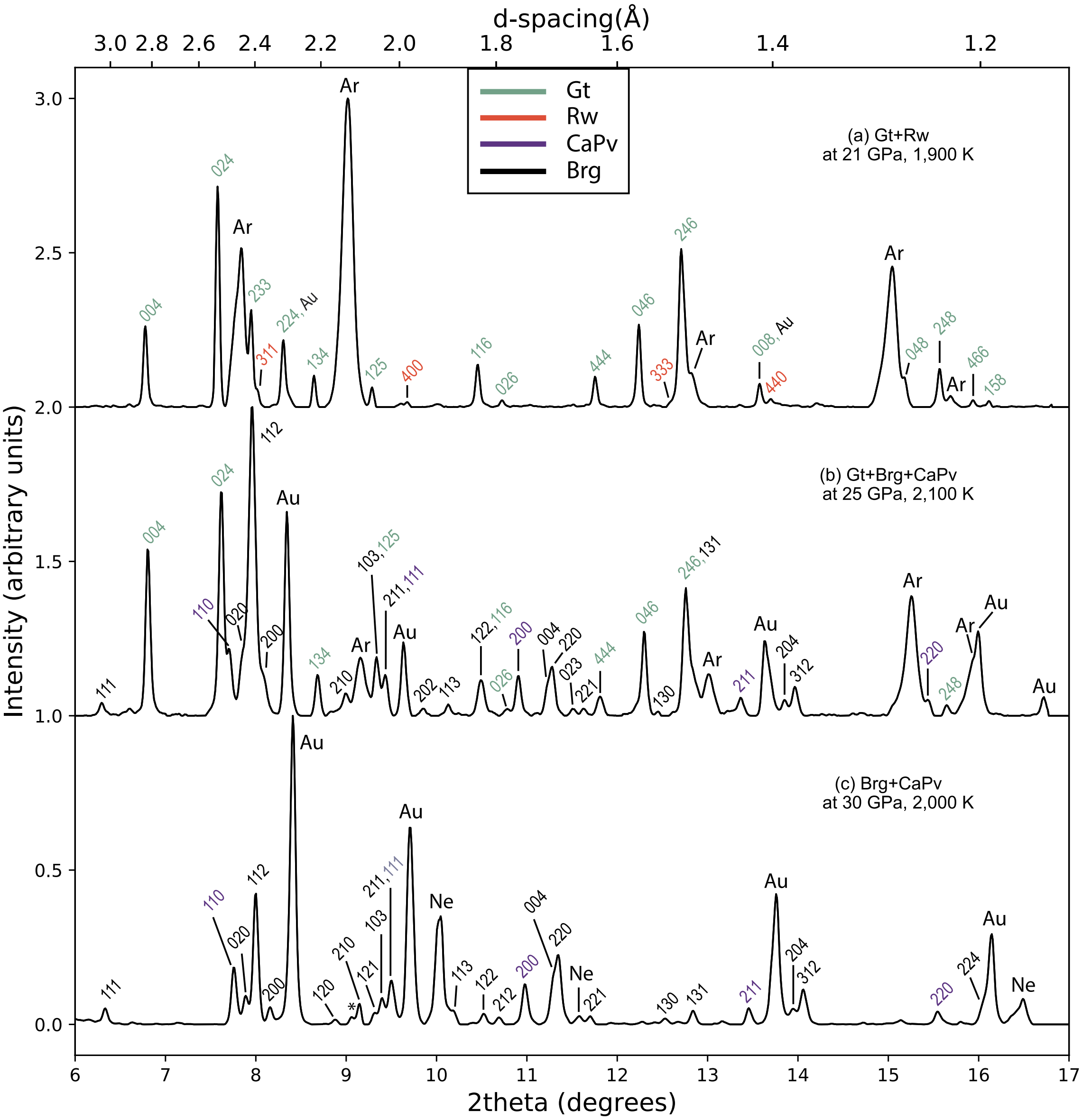

Fig. 2. In-situ X-ray diffraction (XRD) patterns of B30 at high *P–T* in laser-heated diamond anvil cell (LHDAC). X-ray energy was 37 keV. We provided the Miller indices of the major lines. Gt: garnet; Rw: ringwoodite; CaPv: $CaSiO_3$ perovskite; Brg: bridgmanite; Au: gold (pressure standard); Ar: argon (medium); Ne: Neon (medium); and ∗: unidentified peaks.

3.1. *Garnet-dominant P–T field*

Between 19 and 25 GPa, we observed Gt and ringwoodite (Rw) as stable phases (Fig. 2a). The diffraction intensities indicates that Gt represents the major phase of the mineralogy (Fig. 3). We employed the Rietveld refinement using GSAS-II (Toby and Von Dreele, 2013) and obtained 86.5 and 14.5 vol% for Gt and Rw, respectively, which is supported by our STEM observations (Table 2). Fig. 1 shows a high-angle annular dark-field (HDADF) image of the sample from run #4430 which was synthesized at 19.5 GPa (pressure measured at 300 K) and 1900 K in LHDAC. The chemical maps of the image show that Gt exists as matrix that surrounds the Rw grains. From the STEM-EDS images, we obtained 85.3 and 14.7 vol% for the area proportions of Gt and Rw, respectively, consistent with our mass-balance calculation, which yielded 82.7 and 17.3 vol% of Gt and Rw, respectively (Table 2).

$Fe^{3+}/\Sigma Fe$ was not measured for the recovered sample in this study. Because the starting glass was synthesized in the reducing condition, we expect the dominant valence state of Fe is Fe^{2+}. If $Fe^{3+}/\Sigma Fe$ was large in the synthesized samples, the phase proportion of Gt would be even larger because Gt can accommodate the large amount of Fe^{3+} in the crystal structure, unlike Rw (McCammon and Ross, 2003).

The modern MORB mineralogy features Gt as the most abundant component (60–90 vol%) (Irifune and Ringwood, 1993; Litasov and Ohtani, 2005) as does B30 mineralogy (86 vol%; Table 2). However, stable minor phases are significantly different between these two compositions. The (Mg + Fe + Ca)/Si ratio of B30 is higher than 1 (~1.15) and therefore excess MgO and FeO can form Rw in addition to Gt as observed in our experiments. On the other hand, in the modern MORB composition the (Mg + Fe + Ca)/Si ratio is low enough (0.63) to form stishovite (Stv) from excess silica content (Gale et al., 2013). In addition, the greater Al content (15.5 wt%) in modern MORB adds Al-rich phase to the mineralogy, whereas nearly all Al is incorporated in Gt in B30 (8.6 wt%). The mineralogy of the modern MORB composition consists of Gt, Stv, CaPv, and Al-phase, in an order of their abundances, at 15–26 GPa and 1473–2573 K (Irifune et al., 1986; Irifune and Ringwood, 1993; Hirose and Fei, 2002).

At a similar pressure range, pyrolite has Rw (or Wd), Gt, CaPv, and akimotoite (Aki) in an order of abundance (Hirose, 2002; Ye et al.,

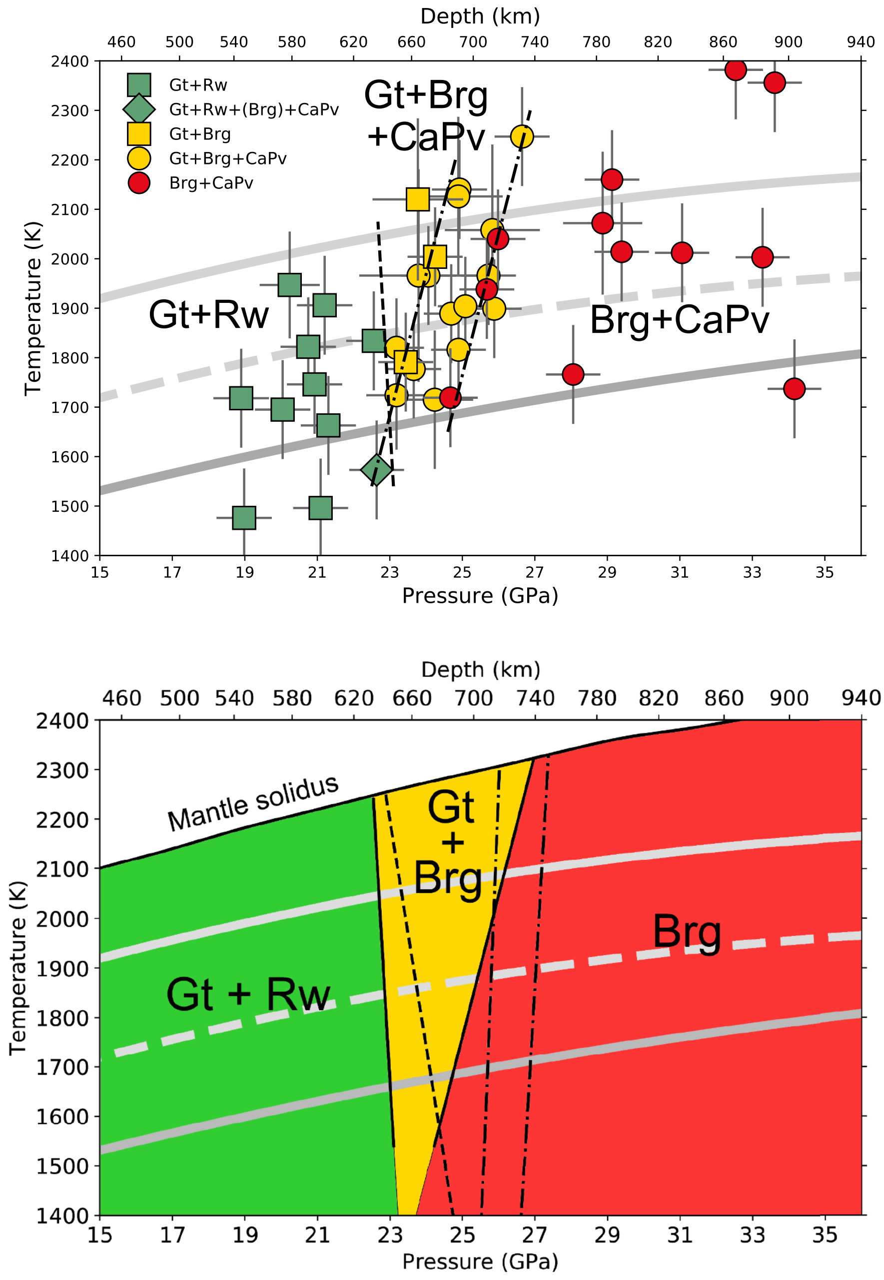

Fig. 3. Phase changes in the B30 composition at high pressure and temperature. The light gray line represents the Archean mantle geotherm, which was shifted by 200 K from the modern mantle geotherm (the dashed gray line; Brown and Shankland, 1981). The gray line represent the temperature profile of the subducting slab after Klein et al. (2017). Top: Each symbol represents one heating cycle in the LHDAC experiments. The dashed and dot-dashed lines indicate the post-spinel and post-Gt transition boundaries determined in this study, respectively. Bottom: The major phases in the distinctive mineralogy fields. The black solid lines are Brg-in and Gt-out boundaries determined in this study. The Brg-in boundary of the post-spinel transition in pyrolite (Hirose, 2002) is plotted as the dashed line. The Brg-in (left) and Gt-out (right) boundaries in modern MORB (Hirose et al., 1999) are plotted as the dot-dashed lines. The mantle solidus is obtained from Andrault et al. (2018b). Gt: garnet; Rw: ringwoodite; CaPv: calcium perovskite; Brg: bridgmanite.

2014; Ishii et al., 2018). Pyrolite has a much higher (Mg + Fe + Ca)/Si ratio (1.49) than modern MORB and B30 (Table 1), making Rw (or Wd) the most abundant phase in the mineralogy. As shown in Table 2, Gt represents 84 vol% in B30, whereas Rw represents 60 vol% in pyrolite (Irifune et al., 2010; Ishii et al., 2018).

The chemical composition of Gt is significantly different among B30, modern MORB, and pyrolite (Table S2). Compared to B30, Gt in modern MORB has twice more Al_2O_3 (8.6 and 20.6 wt%, respectively) and half as many MgO (20.9 and 12.3 wt%, respectively) as B30 has (Hirose and Fei, 2002). Gt in pyrolite has nearly half as much FeO (5.0 and 11.8 wt%, respectively) and CaO (4.6 and 9.0 wt%) as B30 does, but slightly more MgO than in B30 (Hirose, 2002). These compositional differences are important to consider for the density and velocity profiles.

3.2. Garnet-bridgmanite-transition *P–T* field

At intermediate pressures in our experiments, we observed the Gt-Brg-transition *P–T* field in B30 (Fig. 3). Above 23 GPa, Rw disappears and Brg appears, suggesting the occurrence of the post-spinel transition where Rw decomposes into Brg and ferropericlase (Fp). While the diffraction peak intensities show that Gt is still the major phase in the Gt + Brg mineralogy (Fig. 2), we could not resolve Fp in XRD patterns because of the peak overlap with Ar, Gt, or Brg peaks. Furthermore, the peak intensities of Fp is expected to be small because of the possible reduction process in the amount of Fp. Brg is known to have high capacity for Fe^{3+} through the charge disproportionation reaction: 3FeO to $2Fe_2O_3$ and Fe metal (Frost et al., 2004). If a significant fraction of Fe is Fe^{3+}, the more Brg can form by the coupled substitution of Mg^{2+} + Si^{4+} with Fe^{3+} + Al^{3+}, and therefore reduce the available FeO for Fp in the system (e.g., McCammon, 1997; Andrault et al., 2001). We estimated $Fe^{3+}/\Sigma Fe$ in Brg based on the measured compositions by assuming the charge-balanced substitutions of Fe^{3+} and Al^{3+}. The estimation yields approximately 0.57 for $Fe^{3+}/\Sigma Fe$, which is consistent with previous reports (e.g. Shim et al., 2017). However, we note that this estimation method for $Fe^{3+}/\Sigma Fe$ is very sensitive to the Si# in the

Table 2
Chemical compositions of the recovered samples from the Gt-dominant *P–T* field and the Brg-dominant *P–T* field. The compositions were normalized to be 100% in total.

	19.5 GPa†, 1900 K		31 GPa, 2000 K	
wt%	Gt	Rw	Brg	CaPv
SiO_2	49.7	41.4	47.9	48.1
Al_2O_3	8.6	2.7	9.0	1.1
FeO^a	11.8	23.8	13.1	4.6
MgO	20.9	29.2	26.3	3.4
CaO	9.0	2.8	3.7	42.8
Proportions (vol%)				
Mass balance	82.7	17.3	81.6	18.4
EDS mapping	85.3	14.7		
Rietveld	85.5	14.5	82.2	17.8
Average^b (vol%)	84.5	15.5	81.9	18.1

^{a}All Fe is assumed to be Fe^{2+}.
^{b}Averaged proportions from the two different methods.
†Pressure was measured at 300 K.

stoichiometric composition of Brg, and therefore the large uncertainties are involved given the error range of the EDS quantitative analysis (~10%).

We did not observe Fe metal in either STEM observations or XRD patterns, perhaps because of the expected small amount of Fe metal (Section 3.3). Although the limited number of data points increases the uncertainties, the *P–T* slope of Brg-in boundary was roughly estimated to be −0.8 ± 0.3 MPa/K, in a good agreement with the Clapeyron slope of the post-spinel transition from previous studies (e.g. Katsura et al., 2003; Litasov et al., 2005; Ishii et al., 2011, 2018). At higher pressures above 1600 K, CaPv was observed alongside Gt and Brg.

The diffraction peak intensities of Brg are in general stronger in the Gt + Brg + CaPv mineralogy than in the Gt + Brg mineralogy. These observations suggest the post-Gt transition where Gt decomposes into CaPv and Brg. We observed the two phase boundaries for the post-Gt transition with 1.7 GPa of the pressure interval: the CaPv-in boundary and Gt-out boundary. The *P–T* slopes of these boundaries were determined to be 3.5 ± 0.5 MPa/K, which is in the middle of the range of the Clapeyron slopes of the post-Gt transition in previous studies (Hirose et al., 1999; Kubo and Akaogi, 2000; Oguri et al., 2000; Hirose, 2002; Litasov et al., 2004; Ishii et al., 2018). Note that the uncertainties of the *P–T* slopes may be large due to the limited number of data points across the boundaries. The gradual post-Gt transition has been reported by earlier experiments of Al-bearing Gt (Irifune et al., 1996) up to 2.1 GPa of an interval at 1773 K for 3–11 mol% of Al_2O_3. Gt in B30 contains 4.8 mol% of Al_2O_3 which is estimated to yield 1.1 GPa interval for the post-Gt transition according to Irifune et al. (1996). However, Gt in B30 also contains a significant amount of FeO (11.8 wt%; Table 1), the effect of which on the pressure interval of the post-Gt transition is not well known.

The opposite signs of *P–T* slopes of the post-spinel and post-Gt transitions (−0.8 ± 0.3 and 3.5 ± 0.5 MPa/K, respectively) results in the wider stability of the Gt-Brg-transition *P–T* field with an increase in temperature above 1600 K. Below 1600 K, we do not have sufficient number of data points due to the large kinetic effects at lower temperatures. One run at 22.6 GPa and 1570 K (the green diamond in Fig. 3) shows the signs of Brg 112, 200, and 220 lines and strong CaPv 110 line in the XRD pattern, alongside the strong Gt and Rw lines. These observations are in line with CaPv-in boundary observed from the higher temperatures, suggesting that the post-Gt transition may occur at shallower depths than the post-spinel transition at lower temperatures.

The most noticeable difference in mineralogy between modern MORB and B30 at the intermediate pressure range is the depths of Brg-in and Gt-out boundaries (Fig. 3b). For example, at 1700 K Brg-in boundary appears as the post-spinel transition at a lower pressure of 23 GPa in B30 than the post-Gt transition at 25.8 GPa in modern MORB (Hirose et al., 1999). The Si-rich composition of modern MORB does not form Rw in the mineralogy, resulting in the absence of the post-spinel transition, which can occur at the shallower depth than the post-Gt transition. Then, Gt completely transformed to Brg at 24.8 GPa in B30, whereas Gt persists until 26.8 GPa in modern MORB (60–70 vol%) (Hirose et al., 1999; Irifune and Ringwood, 1993; Litasov and Ohtani, 2005). The difference in the depth and the *P–T* slope of Gt-out boundary between B30 and modern MORB is likely caused by the compositional difference in Gt (Table S2).

Pyrolite has similar mineralogy as B30 in the Gt-Brg-transition *P–T* field. In pyrolitic composition, Gt and Brg coexist as major components (Hirose, 2002; Ishii et al., 2018) at 22–26 GPa. Also, pyrolite exhibits the negative slope for Brg-in boundary because of the post-spinel transition. Brg-in boundary appears at a nearly same pressure in B30 and pyrolite: 22.8 and 22.6 GPa at 1900 K, respectively (Ishii et al., 2018). On the other hand, the Gt-out boundary appears at a higher pressure in B30 than in pyrolite by 1.1 GPa: 25.5 and 24.4 GPa at 1900 K, respectively (Ishii et al., 2018).

3.3. Bridgmanite-dominant *P–T* field

At pressures above 25 GPa, the mineralogy of B30 becomes Brg and CaPv (Fig. 3). The diffraction intensities show that Brg is the major phase in the Brg + CaPv system (Fig. 2). The (Mg + Fe + Ca)/Si ratio of B30 is higher than 1 (1.15), the excess MgO and FeO can stabilize Fp together with Brg and CaPv, if the majority of Fe is Fe^{2+}. However, we could not identify Fp peaks in the diffraction patterns because of the expected peak overlap with the Brg peaks. Fp was not observed in TEM analysis either. The amount of Fp might have been too small to be detected because the dispropotionation reaction of Brg (Section 3.2; Frost et al., 2004) can reduce the available number of Fe^{2+} for Fp. Although the heating duration was adequately controlled in our experiments within 8 mins (Table S1), we do not rule out the possibility that the Soret diffusion caused the Fe loss in the heating center (Sinmyo and Hirose, 2010). Some amount of FeO or Fe metal might have migrated away from the heating center to the low-temperature regions.

The calculated phase proportions based on the measured compositions by TEM-EDS (Table 2) yield only 1 ± 1 vol% of Fp. For Brg and CaPv, 81.6 and 18.4 vol% were obtained by the mass-balance calculations, consistent well with 82.2 and 17.8 vol% from Rietveld refinements within 1% of difference (Table 2).

As described in Section 3.1, the starting material was synthesized under a reducing condition. Even if $Fe^{3+}/\Sigma Fe$ was larger in the synthesis products, the phase proportion of Brg would be still large because Brg is the only phase that can incorporate Fe^{3+} in the mineralogy in the Brg-dominant *P–T* field.

Modern MORB contains much lower content of Brg than B30 at *P–T* conditions of the lower-mantle. Modern MORB contains 30, 27, 22, and 21 vol% of CaPv, aluminous phase, Stv, and Brg, respectively at 31 GPa (Ricolleau et al., 2010). Pyrolite and B30 are much alike in that Brg is abundant (75, 18, and 7 vol% for Brg, Fp, and CaPv, respectively, at above 27 GPa for pyrolite; Irifune et al. (2010); Ishii et al. (2018)), but different in that B30 contains very small or no Fp in the mineralogy.

4. Density profiles

4.1. Density profile of Archean volcanic crust

We estimated the density profiles of Archean volcanic crust (B30) along the low and equilibrated temperature profiles in the Archean (hereafter referred to as AL and AE, respectively). The AL temperature was obtained from the temperature model of the subducting slab in Klein et al. (2017). For the AE temperature, we assumed the same temperature as the surrounding mantle in the Archean, which was shifted from the modern mantle geotherm (Brown and Shankland,

1981) by 200 K (Korenaga, 2008; Herzberg et al., 2010). Fig. S2 compares the geotherm models with the adiabatic temperature gradients.

Our in-situ XRD experiments provided the direct measurements of the unit-cell volumes of the stable phases at high *P*–*T*. We considered Gt, Rw, Brg, and CaPv at 20–34 GPa. For the Gt + Rw mineralogy, the chemical compositions and phase proportions of Gt and Rw were obtained from our STEM-EDS measurements, which were assumed to remain unchanged within the same mineralogy field (Table 2). At pressures above Brg-in boundary and below CaPv-in boundary, we took Fp into account the mineralogy (Gt + Brg + Fp) and density calculations. The measured Rw composition was used to model the compositions and proportions of Brg and Fp, which form through the post-spinel transition. The unit-cell volumes of Fp were calculated by the equation of state from Speziale et al. (2007). At pressures above CaPv-in boundary (for the Gt + Brg + CaPv mineralogy), the compositions of Brg and CaPv were obtained from our STEM-EDS measurements and assumed to remain unchanged (Table 2). Their proportions were obtained by mass-balance calculations based on the gradual transformation of Gt into Brg and CaPv. At pressures above Gt-out boundary (for the Brg + CaPv mineralogy), the compositions and proportions of Brg and CaPv were assumed to remain unchanged (Table 2). More information on the density profile model can be found in Text S1.

We also calculated the density of pyrolite in the Archean for comparisons with the B30 density (see Section 4.3 for the method). Fig. 4 shows that the B30 density is greater than the pyrolite density in the Archean at most depths between 20 and 34 GPa (570 and 900 km). The pyrolite density shows a sharp increase at 23–23.5 GPa because of the post-spinel transition, followed by the gradual increase, contributed by the post-Gt transition that occurs in the larger pressure interval (22.5–28 GPa) at the elevated mantle temperature in the Archean.

The similar patterns of the phase transitions are observed in B30. The B30 density along the AE temperature markedly increases over a pressure interval of 25–26 GPa (Fig. 4), because of the phase transformation of Gt and Rw into Brg (Section 3.2). The post-spinel transition in B30 at 23 GPa may not increase the density as much as in pyrolite because the lower proportions of Rw (16 and 60 vol%, respectively; Irifune et al., 2010; Ishii et al., 2018) forms the limited amount of Brg. The B30 density becomes slightly lower than the pyrolite density at 24–25 GPa. However, the Gt-out boundary of the post-Gt transition is at shallower depth in B30 than in pyrolite (26 and 28 GPa, respectively) because of the narrower transition thickness (1.7 GPa of the pressure interval) in B30. As a result, B30 becomes denser than pyrolite by 0.1 g/cm^3 above 25 GPa in the AE temperature (Fig. 6a).

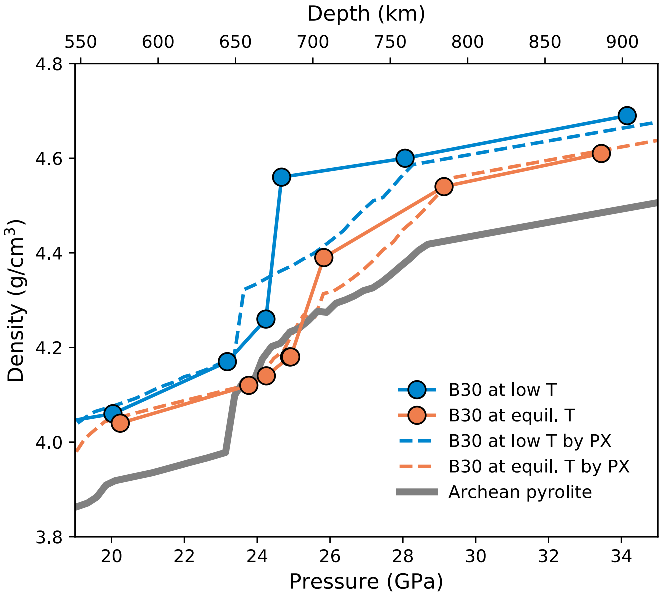

Fig. 4. Density of B30 along different temperature profiles in the Archean. The blue and red lines cirlines represent densities along low (AL), and equilibrated (AE) temperature profiles in the Archean, respectively. The solid and dashed lines indicate densities determined by experiments and by Perple_X (PX; Connolly, 2009), respectively. The circles along the solid lines represent the data points obtained from our experiments. Information on the temperature profiles can be found in Table S3. (For interpretation of the references to color in this figure legend, the reader is referred to the web version of this article.)

In the AL temperature, the B30 density is always greater than the pyrolite density at 20–34 GPa (Fig. 4). The B30 density notably increases at 24–25 GPa because of the post-Gt transition with the narrow pressure interval (1.7 GPa). The density along the AL temperature is greater than along the AE temperature, because of the thermal expansion. On the other hand, the B30 density along the colder temperatures was not investigated in this study due to the limited number of data points at low temperatures. However, we speculate that the B30 density along the colder temperatures should be even greater than the densities in the AE and AL temperatures because the depths of phase transition into Brg will be shallower and the volumes of the phases will be smaller with lower temperatures.

4.2. Comparisons of the B30 density between experiments and Perple_X

To examine possible differences between experiments and theoretical calculations, we used Perple_X (Connolly, 2009) to calculate the densities of B30 for the AL and AE temperatures and compared with our experiments. In Perple_X, we used the Mie-Grüneisun formulation from Stixrude and Lithgow-Bertelloni (2005) and the thermodynamic data of mineral phases from Stixrude and Lithgow-Bertelloni (2011), which has been widely used for multi-phase assemblages in the Earth's mantle conditions (e.g., Nakagawa et al., 2010; Stixrude and Lithgow-Bertelloni, 2012; Klein et al., 2017).

The B30 density appears to be in a good agreement between the experiments and the Perple_X model except for 24.5–28 GPa, where the density from the experiments becomes much greater (Fig. 4). The transition thickness of the post-Gt transition is narrower in the experiments than in the Perple_X model (1.7 and 5 GPa, respectively). The B30 density above 28 GPa in the exepriments is in a good agreement with that in the Perple_X model.

Brg-in boundary is consistent with each other within 1% (23.6 and 23.4 GPa, respectively), whereas the Gt-out boundary is considerably at higher pressure in the Perple_X model than in our experiments (28.1 and 24.8 GPa at 1700 K, respectively). The discrepancy results in the greater density in the experiments than in the Perple_X model at 24.8–28 GPa (Fig. 4). However, the Clapeyron slopes of the post-spinel and post-Gt transitions are in an excellent agreement between the experiments and Perple_X calculations. The experiments yielded -0.8 ± 0.3 and 3.5 ± 0.5 MPa/K, whereas Perple_X predicted -0.81 MPa/K and 3.1 MPa/K for the post-spinel transition and the post-Gt transition, respectively.

On the other hand, the predicted mineralogy by Perple_X was somewhat different from the experiments (Fig. 5). While the major phases, such as, Gt and Brg are the same with different proportions between the experiments and the Perple_X model, the minor phases are additionally predicted from the Perple_X model. For example, in the AL temperature, the Perple_X mineralogy model shows Stv up to 3 vol% together with either Rw or Fp at 21–25 GPa, unlike our experiments (Fig. 5). In the AL and AE temperatures, the Perple_X mineralogy model predicted 10 vol% of calcium-ferrite phase above 26 GPa, which was not observed from the experiments. In addition, the Perple_X mineralogy model shows Fp above 24 GPa up to 5 vol%, which was not observed from the experiments either. This is likely caused by the lack of consideration of Fe^{3+} in Brg from the Perple_X model, which ignores a reduced amount of Fe^{2+} through the charge disproportionation reaction (Section 3.2; Frost et al., 2004). Our stoichiometric estimation of Brg from the experiments yields Fe^{3+}/ΣFe = 57% (Section 3.2), which

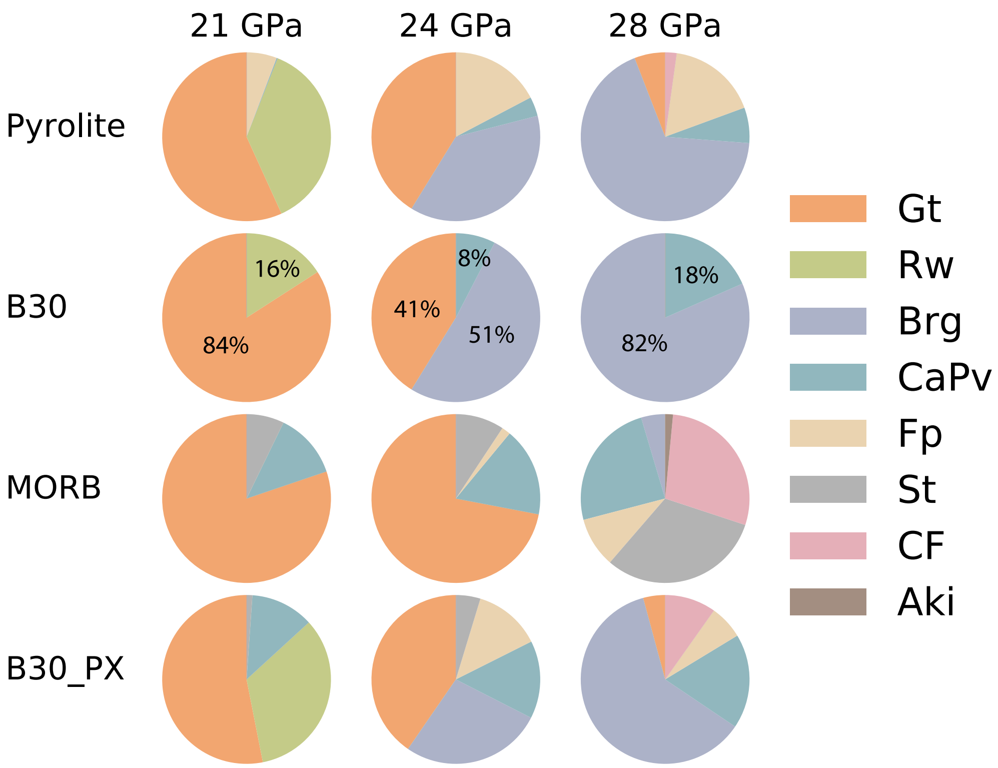

Fig. 5. The mineralogy for pyrolite, B30, MORB in vol% in the MTZ and the topmost lower mantle. The mineralogy of B30 is from the experimental results in this study. Mineralogies of pyrolite, MORB, and B30_PX were calculated using Perple_X (Connolly, 2009) and the data set from Stixrude and Lithgow-Bertelloni (2011). Gt: garnet; Rw: ringwoodite; Brg: bridgmanite; CaPv: $CaSiO_3$ perovskite; Fp: ferropericlase; St: stishovite; CF: calcium ferrite; Aki: Akimotoite.

is in a good agreement with the reported values (Frost et al., 2004; Shim et al., 2017).

4.3. Density difference between the volcanic crust and pyrolite

Fig. 6a,b shows the density difference of B30 and modern MORB with respect to pyrolite (the surrounding mantle) in the Archean and modern day, respectively. The B30 density is directly from our experiments (Section 4.1). The densities of modern MORB and pyrolite were calculated from Perple_X (Section 4.2), which are in an agreement with previous experiments (Irifune and Ringwood, 1993; Hirose, 2002; Irifune et al., 2010; Ishii et al., 2018). The low temperature profiles for modern MORB (hereafter referred to as ML) were obtained from the temperature model of the subducting model (Klein et al., 2017). The equilibrated temperature for modern MORB (ME) was assumed to be same as the surrounding mantle (Brown and Shankland, 1981).

At 23–23.5 GPa, because of the post-spinel transition in pyrolite, the density difference between B30 and pyrolite drops by less than 0.1 g/cm^3. The drop can be seen in modern MORB but with a larger magnitude, 0.2 g/cm^3. The proportions of Rw in pyrolite is much smaller in the Archean than in the modern day (30 and 60 vol%, respectively; Fig.S1), therefore the effect of the post-spinel transition on the density increase is smaller in the Archean. The post-Gt transition in B30 and modern MORB increases the density difference, but occurs at the

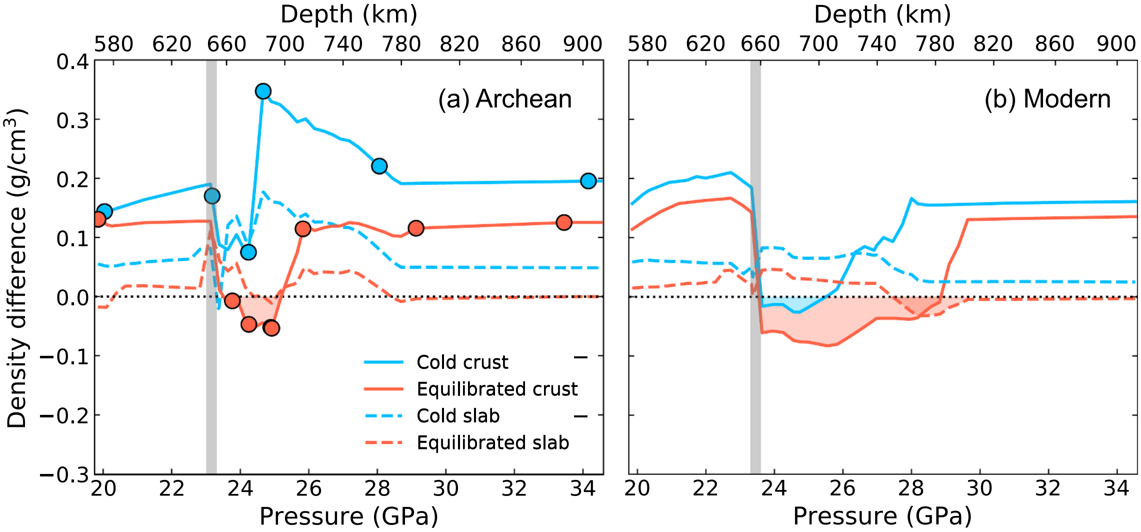

Fig. 6. Density differences of the crusts and subducting slabs with respect to the pyrolitic mantle: (a) B30 and subducting slab in the Archean and (b) MORB and subducting slab in the modern day. The open circles in (a) represent the experimental data points from this study. The vertical gray bars indicate the depth of the post-spinel transition in the pyrolitic mantle. The depths of the negative density contrast are shaded. For subducting slabs, the thicknesses of crust and harzburgite are 40 and 74 km for the Archean, and 7 and 32 km for the modern day, respectively (Text S2). Information on the temperature profiles can be found in Table S3.

different depths. The increase in the density difference occurs at the lower pressures of 24.5–26 GPa in B30 than at 25–29 GPa in modern MORB, depending on the temperature. If thermally equilibrated with the surrounding mantle (i.e. AE or ME), the density difference of B30 becomes negative only at 24–25 GPa (up to -0.03 g/cm^3), whereas that of modern MORB does at 23.5–29 GPa (up to -0.09 g/cm^3). At the deeper depths, B30 maintains the positive density difference by 0.1–0.2 g/cm^3 from the shallow depth than modern MORB does (26 and 29 GPa, respectively).

4.4. Density difference between subducting slabs and pyrolite

We calculated the density of the subducting slab by combining the densities of the crust and harzburgite. The thicknesses of crust and harzburgite are 7 and 32 km for the modern day and 40 and 74 km for the Archean. The detailed descriptions about the density calculations for the subducting slab can be found in Text S2. The density difference of the subducting slab with respect to pyrolite is shown as dashed lines in Fig. 6.

In the Archean, subducting slabs are equal to or denser than pyrolite at most pressures between 20 and 34 GPa (Fig. 6a). For the AL temperature, because of the post-spinel transition in pyrolite, the density difference drops to -0.01 g/cm^3 at 23.3 GPa. For the AE temperature, the drop in the density difference does not appear because of the shallower depth of the post-spinel transition in Archean harzburgite at the higher slab temperature (Text S2). Then, the cold slab maintains the greater density than pyrolite above 28 GPa, while the thermally equilibrated slab becomes equally dense as pyrolite at 29 GPa. On the other hand, the colder slabs are expected to be even denser than the AL and AE slab cases because of the reduced volume at lower temperatures, therefore the greater density difference with respect to pyrolite.

In the modern mantle, the density difference for the ML temperature is always positive at 20–34 GPa (Fig. 6b). In contrast to the AL temperature, the ML temperature does not show the large decrease in density difference at 23.3 GPa although the post-spinel transition occurs at deeper depth in harzburgite of the slab than in pyrolite due to the negative sign of the Clapeyron slope (Fig. S3). In the calculated model, the temperature contrast of the slab along ML temperature with respect to pyrolite is not large enough (~300 K; Text S2) to generate the noticeable difference in the depth of the post-spinel transition between the slab and pyrolite. For even colder slabs in the modern day, the marked decrease in the density difference is expected because of the larger temperature contrast with respect to pyrolite, which will delay the post-spinel transition in the slabs. For the ME temperature, the density difference becomes negative in 27.5–29.6 GPa because of the persistent Gt in modern MORB at the higher slab temperature. Above 30 GPa, the density difference for the ME slab becomes -0.01 g/cm^3.

These results suggest that the contribution from the crustal density is much greater in the Archean than in modern day because of the greater thickness of the crust in the Archean slab (40 and 7 km-thick, respectively).

5. Discussion

5.1. The density behaviors of the volcanic crust and subducting slab in the Archean

We found that Archean volcanic crust (B30) is denser than the pyrolitic mantle at the most depths of the lower MTZ and the shallow lower mantle regardless of the thermal state of the crust, unlike modern MORB (Fig. 6). The different density behaviors of the crust between in the Archean and in the modern day can be attributed to (1) the effect of the Gt composition on the depth of the post-Gt transition in the crust and (2) the temperature effect on the mineralogy of the pyrolitic mantle. First, both Archean volcanic crust and modern MORB have Gt as the most abundant phase (~80 vol%) in the mineralogy. The composition of Gt differs a lot between the two crusts (Table S2), which may affect the depth of the post-Gt transition. For example, the Gt composition in Archean volcanic crust exhibits much smaller Al_2O_3 content than in modern MORB (4.8 and 13.2 mol%, respectively; Table S2). The previous experiments (Irifune et al., 1996) suggested that the Al_2O_3 content may increase the stability of Gt at higher pressure, which is consistent with our observations that Gt-out boundary in Archean volcanic crust is at the shallower depth by 25–50 km-depth (1–2 GPa; Fig. 3) than that in the modern day. Second, the mineralogy of the pyrolitic mantle may be different depending on temperature. Pyrolite shows only 30 vol% of Rw in the hotter Archean, whereas 60 vol% of Rw in the cooler modern day (Fig. S1). The larger Rw proportions in modern-day pyrolite results in the greater increase in the pyrolite density at 660 km-depth through the post-spinel transition. Therefore, the impact on the decrease in the density difference of the crust with respect to the pyrolitic mantle might be much larger in the modern day than in the Archean (Fig. 6).

Our density models of the subducting slab suggest that the effects on the net density of the slab from the less dense harzburgite are smaller in the Archean than in the modern day (Fig. 6). Rather, the greater density of Archean volcanic crust is more effective to the net density of the slab owing to its larger portion in the slab (35 and 18% for Archean volcanic crust and modern MORB, respectively; Table 1). As a result, the density contrast between the subducting slab and the pyrolitic mantle is larger in the Archean than in the modern day (Fig. 6).

5.2. Previous studies on candidates for the subducted Archean volcanic rocks

The exact composition of Archean volcanic crust remains uncertain (Herzberg et al., 2010; Herzberg and Rudnick, 2012). Therefore, it is worthwhile to consider the relevant compositions. The mineralogy and density of komatiite in the MTZ and the topmost lower mantle have been documented by previous studies. Earlier experiments by Nishihara and Takahashi (2001) studied Al-depleted komatiite with (Mg + Fe + Ca)/Si = 1.38 up to 23 GPa. They observed Gt and Rw at 19 GPa, consistent with our experiments on B30 (Section 3.1). The Brg-in boundary is slightly shallower in Al-depleted komatiite by 0.3 GPa than in B30, although their pressure calibration had a large uncertainty at high pressure (Nishihara and Takahashi, 2001). At 21 GPa, Al-depleted komatiite has a much larger proportion of Rw than B30 (40 and 14 vol%, repectively) because of the higher (Mg + Fe + Ca)/Si ratio. At 23 GPa, the stable phases of Al-depleted komatiite are Gt + Brg + CaPv + Fp, consistent with B30 except that we did not find Fp (Section 3.2) because of the lower MgO content in B30 (32.1 and 22.8 wt%, respectively). They estimated the density of Al-depleted komatiite at high *P*–*T* through thermodynamic calculations based on the calculated zero-pressure densities of the phases (Brown and Shankland, 1981). Their results showed the greater density of Al-depleted komatiite than PREM density by 0.02–0.44 g/cm^3 in the upper mantle and the MTZ.

Klein et al. (2017) proposed a model with a komatiitic composition with (Mg + Fe + Ca)/Si = 1.12 that has less MgO than the one used in Nishihara and Takahashi (2001), but similar to B30 in the present study (Table 1). In the thermally equilibrated slab, Gt takes up to 92 vol% with minor CaPv and Fp at 20–23 GPa, but without Rw. Klein et al. (2017) predicted the greater density of komatiite than the pyrolitic mantle in the Archean except when thermally equilibrated. With the equilibrated temperature, the komatiite density becomes smaller than pyrolite at 24–26 GPa, whereas the B30 density is always greater regardless of the slab temperature.

The general conclusions drawn from the previous studies on komatiite (Nishihara and Takahashi, 2001; Klein et al., 2017) concur with this study on B30 in that the greater density of Archean volcanic crust likely facilitates sinking of slabs into the lower mantle.

5.3. The sinking style of Archean volcanic crust and the scale of the mantle mixing

Whether modern-style subduction occurred in the Archean is still under debate (e.g. Van Hunen and Moyen, 2012; Tang et al., 2016; Condie, 2018). Other scenarios for the material transportation into the deep interior in the Archean include the episodic-style subduction (Van Hunen and Moyen, 2012), delamination (Johnson et al., 2014) and shallow subduction (Foley et al., 2003). Van Hunen and Moyen (2012) showed that the high temperature of the mantle would have weakened the harzburgite layer of subducting slabs in the Archean, which would lead to the slab breaking. The frequent break-off of the slabs could have resulted in the episodic-style subduction in the Archean (Van Hunen and Moyen, 2012). The fragments of the slabs would lose some of the driving forces of sinking, such as ridge-push and slab-pull, but we speculate that the slab fragments would keep sinking because of the greater density of the slabs than that of the surrounding mantle in the Archean. Johnson et al. (2014) suggested that the base of Archean volcanic crust could have been gravitationally unstable due to the local thickening, and eventually delaminated by Rayleigh-Taylor instabilities. The delaminated crust would sink because of the greater density than that of the surrounding mantle (Klein et al., 2017). In addition, Foley et al. (2003) proposed that Archean crust would have been recycled to the upper mantle through shallow subduction in the early Archean. The subducting slabs may become stagnant in the upper mantle (Foley et al., 2003). However, it is also possible that the stagnant slabs in the upper mantle break off due to the hot mantle in the Archean (Van Hunen and Moyen, 2012) and sink into the MTZ if the broken slabs are negatively buoyant in the upper mantle (Klein et al., 2017). In any scenario, we speculate that in the Archean, the slabs or crusts would arrive to the 670 km-discontinuity. Even though the slabs or crusts stagnate near the 670 km-discontinuity, they would eventually descend into the lower mantle by Rayleigh-Taylor instabilities.

Once modern-style global subduction had initiated, the volume of the material exchange between the MTZ and lower mantle might have increased. If the subduction transported more materials into the lower mantle with modern-style global subduction, the whole-mantle mixing might have become more efficient. In this case, the mantle mixing with the redox heterogeneities from the lower mantle might have oxidized the upper mantle, eventually leading to the rise of O_2 in the atmosphere toward the GOE (Nicklas et al., 2019; Aulbach and Stagno, 2016; Andrault et al., 2018a).

5.4. The time-dependent changes in the scale of material circulations in the mantle

Since the onset of modern-style global subduction in the Archean (e.g., Laurent et al., 2014; Tang et al., 2016; Condie, 2018), the composition of the subducted volcanic crust have been changed with time. In this view, modern MORB and Archean volcanic crust can represent the two end-members of the crustal compositions (Herzberg et al., 2010; Johnson et al., 2014). As Earth's mantle cools, the composition of the volcanic crust evolves toward the lower (Mg + Fe + Ca)/Si and more Al, and so does the composition of Gt. The change in the Gt composition might have deepen the depth of the post-Gt transition with time. As a result, Gt becomes more stable at a deeper depth, delaying the appearance of Brg, the high-density phase. Also, the thickness of the crust in the slab becomes smaller, and therefore the density contribution from the crust becomes smaller. At the same time, the contribution from the harzburgitic layer becomes greater for the net density of the subducting slab, if slab remains mechanically integrated. As shown in Fig. 6, the subducting slab may have become less denser than the surrounding mantle over time.

Today, seismic tomography images show different states of the modern subducting slabs right beneath the MTZ. Slab stagnation is observed beneath the Western Pacific, whereas subducting slabs seem to directly penetrate into the lower mantle beneath the Central and South American subduction zones (e.g., van der Hilst and Seno, 1993; Fukao et al., 2009; Li and McNamara, 2013; King et al., 2015). As discussed above, the change in the composition and thickness of the crust over time might have reduced the positive density contrast of the subducting slabs, which might partly contribute to the slab stagnation. What we observe from the seismic tomography may be a snapshot of the time-dependent transition of the style of the material circulations between the MTZ and the lower mantle. Therefore, the scale of the mantle mixing may have changed from single-layered since Archean to the two-layered in the future (Klein et al., 2017).

5.5. Archean materials in the present-day mantle

The slow diffusion in the lower mantle (Holzapfel et al., 2005) may have allowed Archean volcanic crust to survive until the present day. Such materials can contribute to the seismic heterogeneities observed in the present-day mantle (Frost et al., 2017; Wu et al., 2019). Particularly, a recent study raised a possibility of an accumulation of ancient oceanic crust at 660 km-depth for the cause of small-scale seismic structures (Wu et al., 2019). In order to evaluate the effect of density on the buoyancy of Archean volcanic crust and Archean subducting slab in the pyrolitic modern mantle, we calculated the densities of B30 and Archean harzburgite. The temperatures for the crust and slab were assumed to be the same as the surrounding mantle, therefore thermally equilibrated (Brown and Shankland, 1981). The B30 density was obtained based on the experimental data (Fig. 3), while those of Archean harzburgite and modern pyrolite were calculated using Perple_X (Connolly, 2009) and the data set from Stixrude and Lithgow-Bertelloni (2011). For Archean subducting slab, we assumed thicknesses of 40 and 74 km-thick for the crust and harzburgitic layer, respectively (Table 1).

We found that B30 remains denser than the pyrolitic mantle by 0.1 g/cm^3 throughout at most depths between 580 and 900 km-depth (Fig. 7). If detached, the density of Archean volcanic crust in the present-day mantle may prefer sinking into the lower mantle to staying at

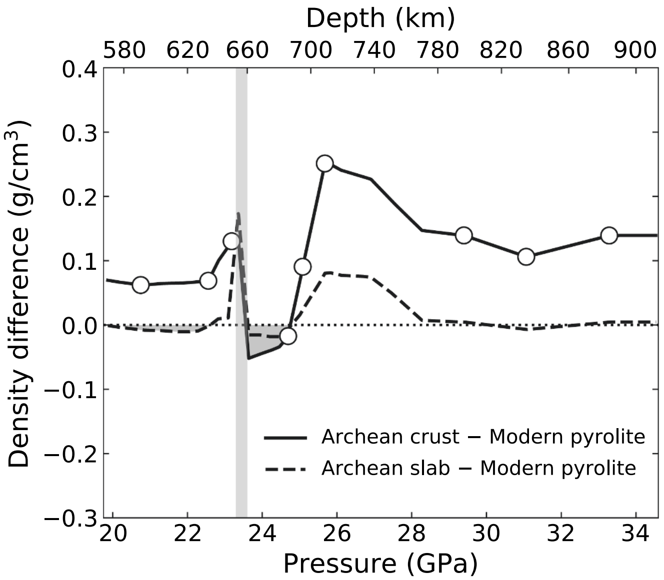

Fig. 7. The density differences of B30 and Archean subducting slab with respect to the pyrolitic mantle in the modern day. The open circles represent our experimental data. The temperatures of B30 and Archean harzburgite were assumed to be equilibrated to modern mantle (Brown and Shankland, 1981). The depth of the post-spinel transition in pyrolite is marked as the vertical gray bar. The densities of Archean harzburgite and pyrolite were calculated using Perple_X (Connolly, 2009) and the data set from Stixrude and Lithgow-Bertelloni (2011).

660 km-depth. In this case, the possible ancient oceanic crust at 660 km-depth that Wu et al. (2019) suggested is unlikely originated from Archean, but more likely sometime close to the present day. For the case of the integrated slab, the density of Archean slab appears to be the same as the modern mantle density at most depths between 580 and 900 km-depth because the lower density of Archean harzburgite cancels out the greater density of B30 (Fig. 7). Therefore, the density effect on the buoyancy of Archean slab in the modern mantle at these depths may be negligible.

5.6. Improving mineralogy modeling for Earth-like planets

From the stellar elemental abundance, we can infer the bulk chemical compositions of the exoplanets around the stars (Bond et al., 2010; Young et al., 2014; Unterborn and Panero, 2017). Such studies have found a surprisingly large range of Mg/Si ratios for the compositions. For the rocky exoplanets, Mg and Si are often assumed to exclusively compose the mantle minerals. Therefore, in order to model the dynamics and structures of the interior of the rocky exoplanets, it is important to have capability to predict mineralogy from a range of different compositions. Because of the large parameteral space and the paucity of experimental data for such a large range of Mg/Si ratio, thermodynamics codes, such as Perple_X, have become important tools to model the mineralogy of the exoplanetary mantle (e.g. Dorn et al., 2015; Unterborn et al., 2017; Vance et al., 2018).

Such thermodynamics codes have successfully reproduced the phase relations observed in experiments for Earth's mantle-related compositions, such as pyrolite and MORB, as also demonstrated in our modeling. Besides these two compositions, there are little data at sufficiently high pressure to examine the predicted models through comparison with experimental data. While the Mg/Si ratio of MORB (0.23; Gale et al., 2013) is too low to be within the possible range of the Mg/Si ratio for Earth-like exoplanets (e.g. 0.8–2 based on the stellar elemental abundances; (Young et al., 2014), that of pyrolite (e.g. Mg/Si = 1.25; McDonough and Sun, 1995) can be useful to infer the mantle mineralogy where Mg out-numbers Si (Mg/Si > 1). Our new data on the B30 composition presented in this study provide the mineralogy with the sufficiently low Mg/Si ratio (0.72), which is an important opportunity to test the modeling capability for the large range of Mg/Si ratio for the possible mantle compositions.

Section 4.2 compares the mineralogy and the density between our experiments and Perple_X model. While the density remains similar to each other at 20–34 GPa (Fig. 4), the minor phases were additionally found in Perple_X model, partly because of the lack of consideration of Fe^{3+}. This difference might be the reason for the different chemical compositions of the major phase, such as Gt, which may in turn result in the different depths of the phase transition (24.8 and 28.1 GPa for the Gt-out boundary in our experiments and Perple_X model, respectively). However, because the density and the major phase are similar between the experiments and Perple_X model for the other pressure ranges (20–24 GPa and 28–34 GPa), we speculate these similarity may continue for the shallower mantle and the deeper mantle. Gt is known to be stable throughout the upper mantle and the MTZ (Irifune et al., 1996), while the Rw composition can exist in other forms of polymorphs, such as olivine and wadsleyite (Nishihara and Takahashi, 2001). In the lower mantle, Brg and CaPv should persist up to ~100 GPa because of the large stability of the perovskite structure (Irifune et al., 2010). Therefore, in spite of some differences in the mineralogy and phase transition behaviors at 25–28 GPa, the use of Perple_X with the data set from Stixrude and Lithgow-Bertelloni (2011) can be effective for modeling the mantle mineralogy and density of Earth-like planets with the low Mg/Si ratio.

6. Conclusion

We have conducted experiments to investigate stable phases and density of Archean volcanic crust in the pyrolitic mantle transition zone and lower mantle. Our experiments showed that Archean volcanic crust is denser than the pyrolitic mantle regardless of temperature, increasing the likelihood of slab penetration across the lower MTZ where modern MORB may experience the slab stagnation beneath some subduction zones. We also modeled the density of the subducting slab in a combination of the densities of the crust and the harzburgitic layer, with respect to the pyrolitic mantle for both the Archean and modern day. The models predicted that the positive density contrast between the subducting slab and the pyrolitic mantle is larger in the Archean than in the modern day. Our results suggest that the density and the large thickness of Archean volcanic crust would have promoted the further sinking into the lower mantle in any tectonic styles. Therefore, the mantle mixing between the MTZ and the lower mantle might have been efficient in the Archean.

CRediT authorship contribution statement

Byeongkwan Ko: Conceptualization, Methodology, Formal analysis, Investigation, Writing - original draft. **Vitali Prakapenka**: Software, Resources, Writing - review & editing. **Martin Kunz**: Software, Resources, Writing - review & editing. **Clemens Prescher**: Software, Resources, Writing - review & editing. **Kurt Leinenweber**: Validation, Writing - review & editing. **Sang-Heon Shim**: Conceptualization, Methodology, Software, Writing - review & editing, Supervision, Funding acquisition.

Acknowledgments

We are grateful for helpful discussions with E. J. Garnero, M. Li, A. K. McNamara, A. D. Anbar, S. J. Desch, C. Till, and R. L. Rudnick. K. Mossman and M. R. Gutierrez assisted with the FIB and STEM measurements at Arizona State University (ASU). Y.-J. Chang and P. Wallace assisted with the FIB and STEM measurements at University of Arizona. This study was supported by NSF (National Science Foundation, the United States) EAR-1725094, NSF EAR-1135452 (the Frontiers of Earth Systems Dynamics (FESD) program), and NASA (National Aeronautics and Space Administration, the United States) NExSS grant NNX15AD53G (PI S. J. Desch). The portions of this work was performed at GeoSoilEnviroCARS (The University of Chicago, Sector 13), Advanced Photon Source (APS), Argonne National Laboratory. GeoSoilEnviroCARS is supported by NSF - Earth Sciences (EAR-1634415) and Department of Energy (DOE) - GeoSciences (DE-FG02-94ER14466). Use of the COMPRES-GSECARS gas loading system was supported by COMPRES under NSF Cooperative Agreement EAR-1606856 and by GSECARS through NSF grant EAR-1634415 and DOE grant DE-FG02-94ER14466. This research used resources of the APS, a U.S. DOE Office of Science User Facility operated for the DOE Office of Science by Argonne National Laboratory under Contract No. DE-AC02-06CH11357. This research used resources of the Advanced Light Source, which is a DOE Office of Science User Facility under contract no. DE-AC02-05CH11231. Beamline 12.2.2 is supported by COMPRES, the Consortium for Materials Properties Research in Earth Sciences under NSF Cooperative Agreement EAR 10-43050. The experimental data are provided as a run table in supplementary material.

Declaration of competing interest

There is no conflict of interest with this study.

Appendix A. Supplementary data

Supplementary data to this article can be found online at https://doi.org/10.1016/j.pepi.2020.106490.

References

Andrault, D., Bolfan-Casanova, N., Guignot, N., 2001. Equation of state of lower mantle (Al, Fe)-MgSiO3 perovskite. Earth Planet. Sci. Lett. 193, 501–508.

Andrault, D., Muñoz, M., Pesce, G., Cerantola, V., Chumakov, A., Kantor, I., Pascarelli, S., Rüffer, R., Hennet, L., 2018a. Large oxygen excess in the primitive mantle could be the source of the great oxygenation event. Geochemical Perspectives Letters 6, 5–10.

Andrault, D., Pesce, G., Manthilake, G., Monteux, J., Bolfan-Casanova, N., Chantel, J., Novella, D., Guignot, N., King, A., Itié, J.P., et al., 2018b. Deep and persistent melt layer in the Archaean mantle. Nature Geoscience 11, 139.

Aulbach, S., Stagno, V., 2016. Evidence for a reducing Archean ambient mantle and its effects on the carbon cycle. Geology 44, 751–754.

Baker, M.B., Beckett, J.R., 1999. The origin of abyssal peridotites: a reinterpretation of constraints based on primary bulk compositions. Earth Planet. Sci. Lett. 171, 49–61.

Bédard, J.H., 2006. A catalytic delamination-driven model for coupled genesis of Archaean crust and sub-continental lithospheric mantle. Geochim. Cosmochim. Acta 70, 1188–1214.

Bond, J.C., O'Brien, D.P., Lauretta, D.S., 2010. The compositional diversity of extrasolar terrestrial planets. I. In situ simulations. The Astrophysical Journal 715, 1050.

Brown, J., Shankland, T., 1981. Thermodynamic parameters in the earth as determined from seismic profiles. Geophys. J. Int. 66, 579–596.

Christensen, U.R., 1997. Influence of chemical buoyancy on the dynamics of slabs in the transition zone. Journal of Geophysical Research: Solid Earth 102, 22435–22443. https://doi.org/10.1029/97jb01342.

Condie, K.C., 2018. A planet in transition: the onset of plate tectonics on Earth between 3 and 2 Ga? Geosci. Front. 9, 51–60.

Connolly, J., 2009. The geodynamic equation of state: what and how. Geochem. Geophys. Geosyst. 10.

Davies, G.F., 2008. Episodic layering of the early mantle by the "basalt barrier" mechanism. Earth and Planetary Science Letters 275, 382–392. URL: http://dx.doi.org/10.1016/j.epsl.2008.08.036, doi: https://doi.org/10.1016/j.epsl.2008.08.036.

Dorn, C., Khan, A., Heng, K., Connolly, J.A., Alibert, Y., Benz, W., Tackley, P., 2015. Can we constrain the interior structure of rocky exoplanets from mass and radius measurements? Astronomy & Astrophysics 577, A83.

Dorogokupets, P., Dewaele, A., 2007. Equations of state of MgO, Au, Pt, NaCl-B1, and NaCl-B2: internally consistent high-temperature pressure scales. High Pressure Res. 27, 431–446.

Foley, S.F., Buhre, S., Jacob, D.E., 2003. Evolution of the Archaean crust by delamination and shallow subduction. Nature 421, 249.

Frost, D.J., Liebske, C., Langenhorst, F., McCammon, C.A., Trønnes, R.G., Rubie, D.C., 2004. Experimental evidence for the existence of iron-rich metal in the Earth's lower mantle. Nature 428, 409.

Frost, D.A., Rost, S., Garnero, E.J., Li, M., 2017. Seismic evidence for Earth's crusty deep mantle. Earth Planet. Sci. Lett. 470, 54–63.

Fukao, Y., Obayashi, M., 2013. Subducted slabs stagnant above, penetrating through, and trapped below the 660 km discontinuity. Journal of Geophysical Research: Solid Earth 118, 5920–5938.

Fukao, Y., Obayashi, M., Nakakuki, T., Group, D.S.P., 2009. Stagnant slab: a review. Annu. Rev. Earth Planet. Sci. 37, 19–46.

Gale, A., Dalton, C.A., Langmuir, C.H., Su, Y., Schilling, J.G., 2013. The mean composition of ocean ridge basalts. Geochem. Geophys. Geosyst. 14, 489–518.

Herzberg, C., Rudnick, R., 2012. Formation of cratonic lithosphere: an integrated thermal and petrological model. Lithos 149, 4–15.

Herzberg, C., Asimow, P.D., Arndt, N., Niu, Y., Lesher, C., Fitton, J., Cheadle, M., Saunders, A., 2007. Temperatures in ambient mantle and plumes: constraints from basalts, picrites, and komatiites. Geochem. Geophys. Geosyst. 8.

Herzberg, C., Condie, K., Korenaga, J., 2010. Thermal history of the Earth and its petrological expression. Earth Planet. Sci. Lett. 292, 79–88.

Hirose, K., 2002. Phase transitions in pyrolitic mantle around 670-km depth: implications for upwelling of plumes from the lower mantle. Journal of Geophysical Research: Solid Earth 107.

Hirose, K., Fei, Y., 2002. Subsolidus and melting phase relations of basaltic composition in the uppermostlower mantle. Geochim. Cosmochim. Acta 66, 2099–2108.

Hirose, K., Fei, Y., Ma, Y., Mao, H.K., 1999. The fate of subducted basaltic crust in the Earth's lower mantle. Nature 397, 53.

Hirose, K., Takafuji, N., Sata, N., Ohishi, Y., 2005. Phase transition and density of subducted MORB crust in the lower mantle. Earth Planet. Sci. Lett. 237, 239–251.

Holland, T., Redfern, S., 1997. UNITCELL: a nonlinear least-squares program for cell-parameter refinement and implementing regression and deletion diagnostics. J. Appl. Crystallogr. 30, 84.

Holzapfel, C., Rubie, D.C., Frost, D.J., Langenhorst, F., 2005. Fe-Mg interdiffusion in (Mg, Fe) SiO3 perovskite and lower mantle reequilibration. Science 309, 1707–1710.

Irifune, T., Ringwood, A., 1993. Phase transformations in subducted oceanic crust and buoyancy relationships at depths of 600–800 km in the mantle. Earth Planet. Sci. Lett. 117, 101–110.

Irifune, T., Sekine, T., Ringwood, A., Hibberson, W., 1986. The eclogite-garnetite transformation at high pressure and some geophysical implications. Earth Planet. Sci. Lett. 77, 245–256.

Irifune, T., Koizumi, T., Ando, J.i., 1996. An experimental study of the garnet-perovskite transformation in the system MgSiO3-Mg3Al2Si3O12. Phys. Earth Planet. Inter. 96, 147–157.

Irifune, T., Shinmei, T., McCammon, C.A., Miyajima, N., Rubie, D.C., Frost, D.J., 2010. Iron partitioning and density changes of pyrolite in Earth's lower mantle. Science 327, 193–195.

Ishii, T., Kojitani, H., Akaogi, M., 2011. Post-spinel transitions in pyrolite and Mg2SiO4 and akimotoite–perovskite transition in MgSiO3: precise comparison by high-pressure high-temperature experiments with multi-sample cell technique. Earth Planet. Sci. Lett. 309, 185–197.

Ishii, T., Huang, R., Fei, H., Koemets, I., Liu, Z., Maeda, F., Yuan, L., Wang, L., Druzhbin, D., Yamamoto, T., et al., 2018. Complete agreement of the post-spinel transition with the 660-km seismic discontinuity. Sci. Rep. 8, 6358.

Ito, Y., Toriumi, M., 2010. Silicon self-diffusion of MgSiO3 perovskite by molecular dynamics and its implication for lower mantle rheology. Journal of Geophysical Research: Solid Earth 115.

Johnson, T.E., Brown, M., Kaus, B.J., VanTongeren, J.A., 2014. Delamination and recycling of Archaean crust caused by gravitational instabilities. Nat. Geosci. 7, 47.

Kasting, J.F., 2013. What caused the rise of atmospheric O2? Chem. Geol. 362, 13–25.

Katsura, T., Yamada, H., Shinmei, T., Kubo, A., Ono, S., Kanzaki, M., Yoneda, A., Walter, M.J., Ito, E., Urakawa, S., et al., 2003. Post-spinel transition in Mg2SiO4 determined by high *P–T* in situ X-ray diffractometry. Phys. Earth Planet. Inter. 136, 11–24.

King, S.D., Frost, D.J., Rubie, D.C., 2015. Why cold slabs stagnate in the transition zone. Geology 43, 231–234.

Klein, B.Z., Jagoutz, O., Behn, M.D., 2017. Archean crustal compositions promote full mantle convection. Earth and Planetary Science Letters 474, 516–526. https://doi.org/10.1016/j.epsl.2017.07.003.

Korenaga, J., 2008. Urey ratio and the structure and evolution of Earth's mantle. Rev. Geophys. 46.

Kubo, A., Akaogi, M., 2000. Post-garnet transitions in the system Mg4Si4O12–Mg3Al2Si3O12 up to 28 GPa: phase relations of garnet, ilmenite and perovskite. Phys. Earth Planet. Inter. 121, 85–102.

Laurent, O., Martin, H., Moyen, J.F., Doucelance, R., 2014. The diversity and evolution of late-Archean granitoids: evidence for the onset of "modern-style" plate tectonics between 3.0 and 2.5 Ga. Lithos 205, 208–235.

Letoullec, R., Pinceaux, J., Loubeyre, P., 1988. The membrane diamond anvil cell: a new device for generating continuous pressure and temperature variations. International Journal of High Pressure Research 1, 77–90.

Li, M., McNamara, A.K., 2013. The difficulty for subducted oceanic crust to accumulate at the Earth's core-mantle boundary. Journal of Geophysical Research: Solid Earth 118, 1807–1816.

Litasov, K.D., Ohtani, E., 2005. Phase relations in hydrous MORB at 18–28GPa: implications for heterogeneity of the lower mantle. Physics of the Earth and Planetary Interiors 150, 239–263. https://doi.org/10.1016/j.pepi.2004.10.010.

Litasov, K., Ohtani, E., Suzuki, A., Kawazoe, T., Funakoshi, K., 2004. Absence of density crossover between basalt and peridotite in the cold slabs passing through 660 km discontinuity. Geophys. Res. Lett. 31.

Litasov, K., Ohtani, E., Sano, A., Suzuki, A., Funakoshi, K., 2005. In situ X-ray diffraction study of post-spinel transformation in a peridotite mantle: implication for the 660-km discontinuity. Earth Planet. Sci. Lett. 238, 311–328.

McCammon, C., 1997. Perovskite as a possible sink for ferric iron in the lower mantle. Nature 387, 694.

McCammon, C., Ross, N., 2003. Crystal chemistry of ferric iron in (Mg, Fe)(Si, Al) O3 majorite with implications for the transition zone. Phys. Chem. Miner. 30, 206–216.

McDonough, W.F., Sun, S.S., 1995. The composition of the Earth. Chem. Geol. 120, 223–253.

Nakagawa, T., Tackley, P.J., Deschamps, F., Connolly, J.A., 2010. The influence of MORB and harzburgite composition on thermo-chemical mantle convection in a 3-d spherical shell with self-consistently calculated mineral physics. Earth and Planetary Science Letters 296, 403–412. https://doi.org/10.1016/j.epsl.2010.05.026.

Newville, M., Stensitzki, T., Allen, D.B., Rawlik, M., Ingargiola, A., Nelson, A., 2016. Lmfit: Non-linear Least-Square Minimization and Curve-Fitting for Python. Astrophysics Source Code Library.

Nicklas, R.W., Puchtel, I.S., Ash, R.D., Piccoli, P.M., Hanski, E., Nisbet, E.G., Waterton, P., Pearson, D.G., Anbar, A.D., 2019. Secular mantle oxidation across the Archean-Proterozoic boundary: evidence from V partitioning in komatiites and picrites. Geochim. Cosmochim. Acta 250, 49–75.

Nishihara, Y., Takahashi, E., 2001. Phase relation and physical properties of an Al-depleted komatiite to 23 GPa. Earth Planet. Sci. Lett. 190, 65–77.

Ogawa, M., 2003. Chemical stratification in a two-dimensional convecting mantle with magmatism and moving plates. Journal of Geophysical Research 108. https://doi.org/10.1029/2002JB002205.

Oguri, K., Funamori, N., Uchida, T., Miyajima, N., Yagi, T., Fujino, K., 2000. Post-garnet transition in a natural pyrope: a multi-anvil study based on in situ X-ray diffraction and transmission electron microscopy. Phys. Earth Planet. Inter. 122, 175–186.

Palin, R.M., White, R.W., 2016. Emergence of blueschists on Earth linked to secular changes in oceanic crust composition. Nat. Geosci. 9, 60.

Prakapenka, V., Kubo, A., Kuznetsov, A., Laskin, A., Shkurikhin, O., Dera, P., Rivers, M., Sutton, S., 2008. Advanced flat top laser heating system for high pressure research at GSECARS: application to the melting behavior of germanium. High Pressure Res. 28, 225–235.

Prescher, C., Prakapenka, V.B., 2015. DIOPTAS: a program for reduction of two-dimensional X-ray diffraction data and data exploration. High Pressure Research 35, 223–230. https://doi.org/10.1080/08957959.2015.1059835.

Ricolleau, A., Perrillat, J.p., Fiquet, G., Daniel, I., Matas, J., Addad, A., Menguy, N., Cardon, H., Mezouar, M., Guignot, N., 2010. Phase relations and equation of state of a natural MORB: implications for the density profile of subducted oceanic crust in the Earth's lower mantle. Journal of Geophysical Research: Solid Earth 115.

Ringwood, A.E., Irifune, T., 1988. Nature of the 650–km seismic discontinuity: implications for mantle dynamics and differentiation. Nature 331, 131.

Rivers, M., Prakapenka, V.B., Kubo, A., Pullins, C., Holl, C.M., Jacobsen, S.D., 2008. The COMPRES/GSECARS gas-loading system for diamond anvil cells at the Advanced Photon Source. High Pressure Res. 28, 273–292.

Schulz, K., 1982. Magnesian Basalts From the Archaean Terrains of Minnesota. George Allen & Unwin, Komatiites. London, pp. 171–186.

Shim, S.H., 2017a. A. PeakPo - A Python Software for X-ray Diffraction Analysis at High Pressure and High Temperature. https://doi.org/10.5281/zenodo.842949.

Shim, S.H., 2017b. B. Pytheos -A Python Tool Set for Equations of State Pytheos - A Python Tool Set for Equations of State. https://doi.org/10.5281/zenodo.802392.

Shim, S.H., Grocholski, B., Ye, Y., Alp, E.E., Xu, S., Morgan, D., Meng, Y., Prakapenka, V.B., 2017. Stability of ferrous-iron-rich bridgmanite under reducing midmantle conditions. Proc. Natl. Acad. Sci. 114, 6468–6473.

Sinmyo, R., Hirose, K., 2010. The soret diffusion in laser-heated diamond-anvil cell. Phys. Earth Planet. Inter. 180, 172–178.

Speziale, S., Lee, V., Clark, S., Lin, J., Pasternak, M., Jeanloz, R., 2007. Effects of fe spin transition on the elasticity of (Mg, Fe) O magnesiowüstites and implications for the seismological properties of the Earth's lower mantle. Journal of Geophysical Research: Solid Earth 112.

Stixrude, L., Lithgow-Bertelloni, C., 2005. Thermodynamics of mantle minerals—I. Physical properties. Geophys. J. Int. 162, 610–632.

Stixrude, L., Lithgow-Bertelloni, C., 2011. Thermodynamics of mantle minerals-II. Phase equilibria. Geophys. J. Int. 184, 1180–1213.

Stixrude, L., Lithgow-Bertelloni, C., 2012. Geophysics of chemical heterogeneity in the mantle. Annu. Rev. Earth Planet. Sci. 40, 569–595.

Tang, M., Chen, K., Rudnick, R.L., 2016. Archean upper crust transition from mafic to felsic marks the onset of plate tectonics. Science 351, 372–375.

Tangeman, J.A., Phillips, B.L., Navrotsky, A., Weber, J., Hixson, A.D., Key, T.S., 2001. Vitreous forsterite (Mg2SiO4): synthesis, structure, and thermochemistry. Geophys. Res. Lett. 28, 2517–2520.

Toby, B.H., Von Dreele, R.B., 2013. GSAS-II: the genesis of a modern open-source all purpose crystallography software package. J. Appl. Crystallogr. 46, 544–549.

Unterborn, C.T., Panero, W.R., 2017. The effects of Mg/Si on the exoplanetary refractory oxygen budget. Astrophys. J. 845, 61.

Unterborn, C.T., Desch, S.J., Hinkel, N.R., Lorenzo Jr., A., 2017. Inward Migration of the TRAPPIST-1 Planets as Inferred From Their Water-Rich Compositions. (arXiv preprint arXiv:1706.02689).

van der Hilst, R., Seno, T., 1993. Effects of relative plate motion on the deep structure and penetration depth of slabs below the Izu-Bonin and Mariana island arcs. Earth Planet. Sci. Lett. 120, 395–407.

Van Hunen, J., Moyen, J.F., 2012. Archean subduction: fact or fiction? Annu. Rev. Earth Planet. Sci. 40, 195–219.

Vance, S.D., Panning, M.P., Stähler, S., Cammarano, F., Bills, B.G., Tobie, G., Kamata, S., Kedar, S., Sotin, C., Pike, W.T., et al., 2018. Geophysical investigations of habitability in ice-covered ocean worlds. Journal of Geophysical Research: Planets 123, 180–205.

Wu, W., Ni, S., Irving, J.C., 2019. Inferring Earth's discontinuous chemical layering from the 660-kilometer boundary topography. Science 363, 736–740.

Xu, W., Lithgow-Bertelloni, C., Stixrude, L., Ritsema, J., 2008. The effect of bulk composition and temperature on mantle seismic structure. Earth Planet. Sci. Lett. 275, 70–79.

Xu, J., Yamazaki, D., Katsura, T., Wu, X., Remmert, P., Yurimoto, H., Chakraborty, S., 2011. Silicon and magnesium diffusion in a single crystal of MgSiO3 perovskite. Journal of Geophysical Research: Solid Earth 116.

Ye, Y., Gu, C., Shim, S.H., Meng, Y., Prakapenka, V., 2014. The postspinel boundary in pyrolitic compositions determined in the laser-heated diamond anvil cell. Geophys. Res. Lett. 41, 3833–3841.

Ye, Y., Prakapenka, V., Meng, Y., Shim, S.H., 2017. Intercomparison of the gold, platinum, and MgO pressure scales up to 140 GPa and 2500 K. Journal of Geophysical Research: Solid Earth 122, 3450–3464.

Young, P.A., Desch, S.J., Anbar, A.D., Barnes, R., Hinkel, N.R., Kopparapu, R., Madhusudhan, N., Monga, N., Pagano, M.D., Riner, M.A., et al., 2014. Astrobiological stoichiometry. Astrobiology 14, 603–626.